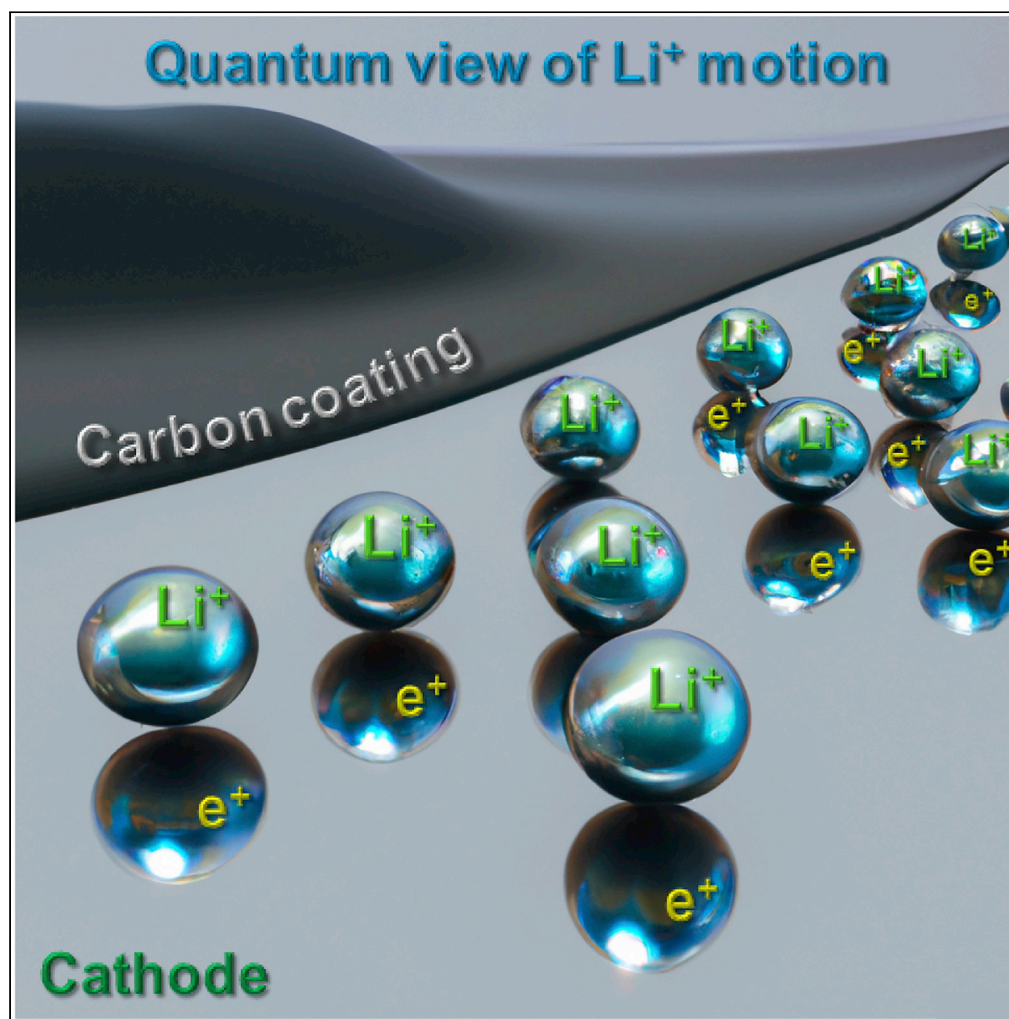**CellPress**

Article

Quantum view of Li-ion high mobility at carbon-coated cathode interfaces

Gioele Pagot, Vito Di Noto, Keti Vezzù, ..., Meiying Zheng, Xin Li, Rafael Ferragut

gioele.pagot@unipd.it (G.P.)
vito.dinoto@unipd.it (V.D.N.)
rafael.ferragut@polimi.it (R.F.)

Highlights

Lithium cobalt oxide cathode nanoparticles are coated with different carbon materials

BES studies demonstrate that only a fraction of lithium ions is mobile

PAS investigations reveal that positrons act as a quantum analogue of lithium ions

BES and PAS demonstrate that carbon influences Li$^+$ mobility in bulk nanoparticles

iScience

Article

Quantum view of Li-ion high mobility at carbon-coated cathode interfaces

Gioele Pagot,[1,*] Vito Di Noto,[1,6,*] Keti Vezzù,[1] Bernardo Barbiellini,[2,3] Valerio Toso,[4,5] Alberto Caruso,[4] Meiying Zheng,[2,4] Xin Li,[2,4] and Rafael Ferragut[4,5,*]

SUMMARY

Lithium-ion batteries (LIBs) are among the most promising power sources for electric vehicles, portable electronics and smart grids. In LIBs, the cathode is a major bottleneck, with a particular reference to its low electrical conductivity and Li-ion diffusivity. The coating with carbon layers is generally employed to enhance the electrical conductivity and to protect the active material from degradation during operation. Here, we demonstrate that this layer has a primary role in the lithium diffusivity into the cathode nanoparticles. Positron is a useful quantum probe at the electroactive materials/carbon interface to sense the mobility of Li-ion. Broadband electrical spectroscopy demonstrates that only a small number of Li-ions are moving, and that their diffusion strongly depends on the type of carbon additive. Positron annihilation and broadband electrical spectroscopies are crucial complementary tools to investigate the electronic effect of the carbon phase on the cathode performance and Li-ion dynamics in electroactive materials.

INTRODUCTION

In recent decades, Li-ion batteries[1–4] have proven to be one of the most promising chemical-to-electrical energy converters for power electronic devices.[5–8] The increasing demand for high performing devices always includes higher power and energy densities, excellent charge-discharge cycle performance and more safety. A key element limiting battery performance is the cathode,[9,10] having a low Li-ion mobility in the bulk.[11] As of today, cathode carbon coating is deemed to boost the transport of electrons through the active nanoparticles,[12–15] and to offer a physical protecting layer against the chemical degradation on cycling.[16,17] The only strategy that has been demonstrated to be valuable to improve the Li-ion mobility in the bulk material, without modifying the cathode chemical composition, is the active nanoparticles downsizing.[11,18] In this way, a shorter pathway is required for Li-ions to enter the cathode nanoparticle full volume, thus enhancing the material rate capabilities. Studies of the cathode electric response and Li$^+$ dynamics are rarely performed on pristine electrode,[19] because full- or half-cells are commonly investigated.[20,21] In these studies, improvements of 1-2 orders of magnitude in the Li-ion diffusion coefficient are obtained after coating with carbon or other composite materials.[12,20,21] However, with this cell configuration a cathode electrolyte interphase (CEI) layer is formed on the surface of nanoparticles on the chemical contact with the electrolyte. The CEI gives a contribution to the material electric response, which limits the other interfaces information (*i.e.*, carbon/LiCoO$_2$) extracted from the experiments.

This work gives the fundamental understanding at the atomic scale of the carbon coating role to achieve ultrafast Li-ion mobility in cathodes. Broadband electrical spectroscopy (BES) and positron annihilation spectroscopy (PAS) are used to study the Li-based battery cathodes. The pristine cathode is prepared by mixing LiCoO$_2$ with the PVDF polymer binder, without the addition of carbon (*NoC*). The other cathodes are obtained by coating the LiCoO$_2$ nanoparticles with carbon: Super P (*SP*), nanospheres (*XC*) and nanotubes (*NT*).

RESULTS AND DISCUSSION

Broadband electrical spectroscopy studies

The interactions between carbon and LiCoO$_2$ (LCO) can be probed with BES studies. This is a useful tool to detect the dependence of the electric response of the cathodes on the structural relaxations and polarization phenomena of materials, which are modulated by the interfaces formed between carbon and LCO

[1]Section of Chemistry for the Technology (ChemTech), Department of Industrial Engineering, University of Padova, Via Marzolo 9, 35131 Padova, Italy

[2]Physics Department, School of Engineering Science, LUT-University, 53851 Lappeenranta, Finland

[3]Department of Physics, Northeastern University, Boston, MA 02115, USA

[4]L-NESS and Department of Physics, Politecnico di Milano, Via Anzani 42, 22100 Como, Italy

[5]INFN Milan Unit, Via Celoria 16, 20133 Milano, Italy

[6]Lead contact

*Correspondence:
gioele.pagot@unipd.it (G.P.),
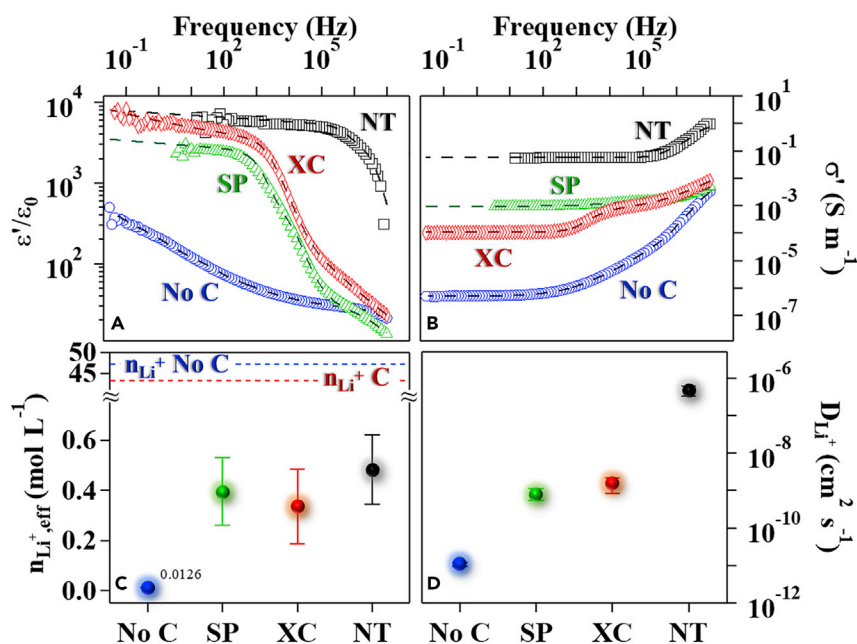vito.dinoto@unipd.it (V.D.N.),
rafael.ferragut@polimi.it (R.F.)

https://doi.org/10.1016/j.isci.2022.105794

Figure 1. Broadband electrical spectroscopy results

Real permittivity (ε', A) and conductivity (σ', B) spectra on frequency of the four different samples containing $LiCoO_2$, PVDF and: without carbon (*No C*, blue circles), carbon Super P (*SP*, green triangles), carbon nanospheres (*XC*, red diamonds), and carbon nanotubes (*NT*, black squares). Markers represent experimental data and dashed lines are the fitting results. Concentration of effective mobile lithium ions ($n_{Li^+ eff}$, C) and lithium diffusion coefficient (D_{Li^+}, D) as a function of the carbon employed into the cathode electrode. Error bars (2 *sigma*) are calculated on the basis of the fitting error and experimental data accuracy. Dotted lines in C represent the total lithium ion concentration in the electrodes with (red line) and without (blue line) carbon.

nanoparticles. A detailed description of the BES theory and the obtained results are in the method details section. A summary of the real permittivity and conductivity spectra of the four investigated cathode materials is reported in Figures 1A and 1B. Their full results are shown in Figures S1–S4 of the supplemental information. To separate the contribution of each polarization phenomenon and dielectric relaxation event, the electric response is analyzed using Equations 6 and 7 (see the method details section). All the samples reveal the presence of several polarization phenomena: (1) σ_1 is the electrode polarization, attributed to the Li-ion accumulation at the interface between cathode and Pt electrodes of the measuring cell; and (2) σ_k (k > 1) are the interdomain polarizations, which correspond to the charge accumulation at the interface between domains in bulk cathode materials with different permittivity, *i.e.*, LCO-PVDF, LCO-carbon interfaces in bulk cathode particles with different shape and/or size. The observed dielectric relaxations (ε_f) are assigned to the host LCO material dynamics. In particular, these modes are associated with the fluctuating dipole moments of the distorted octahedra of 3D LCO involving metal-oxygen bonds, coupled with carbon matrix relaxations. Indeed, it has been demonstrated that the 3D structure of cathode materials is dynamic.[22] Coupling this latter structural flexibility with elementary Li^+ ion migration events results in an enhanced Li-ion diffusion in 3D material.[22,23] BES studies establish that the carbon layer formed on the LCO surface has a primary role in the dynamics and in the long-range charge migration processes occurring in the cathode. The real permittivity has a sharp increase of 1-2 orders of magnitude as the carbon component is added into the samples (Figure 1A). The same is observed for the real conductivity spectra (Figure 1B) and for the obtained fitting results related to the conductivity and relaxation frequency of the polarization phenomena associated with the Li-ion conduction (Table S1 in supplemental information). This gives a clear indication that the carbon layer is not a simple current collector but its interaction with LCO particles plays a very complex and primary role in the dynamics and percolation activation of charges at the carbon/LCO interface. This is likely the result of a significant electronic interaction existing at the interface between carbon and the functionalities of LCO at the surface. The physico-chemical and morphological properties of the carbon material seem to differently influence the observed behaviors, thus revealing that the selection of the carbon matrix is challenging. Therefore, to maximize the battery performance, it is crucial to dispose of suitable techniques to study these types of interactions.
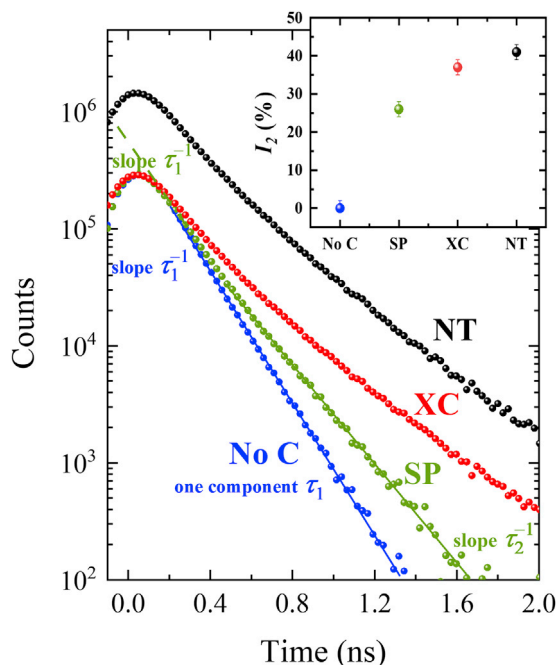
Figure 2. Positron lifetime spectra of LiCoO$_2$ cathodes

The spectra of *SP, XC, NT* and *No C* cathodes are normalized at the same high peak after subtracting the source and spurious components (*NT* spectrum is multiplied by a factor of 5 to avoid overlapping with *XC* spectrum). The inset shows the intensity of the second lifetime component I_2 as a function of the carbon employed to coat the cathode grains (see Table 1). Error bars are calculated on the basis of the experimental errors.

The Li-ion mobility into a solid crystalline material is strongly hindered, differently from what is observed in a system such as an aqueous electrolyte containing ions. Indeed, the actual number of really mobile species differs from that of the total of charges present into the host matrix. In our case, the total Li$^+$ concentration in active cathode material is 47 mol L^{-1}, whereas in the carbon-based cathodic materials is 43 mol L^{-1}. In practice, the effective concentration of mobile Li-ions in the cathode bulk materials ($n_{Li^+ eff}$) shown in Figure 1C (see Table S1) can be determined combining BES studies and electric response results of cathode materials by using Equation 8 (see the method details section). As expected, $n_{Li^+ eff}$ is lower than the stoichiometric Li$^+$ content value of cathodic materials (*ca.* 45 mol L^{-1}): (1) of a factor of 10^2 for carbon-based cathode materials; and (2) of more than three orders of magnitude lower for *No C* sample. This is clear evidence that the addition of carbon to the active material does not only enhance its electrical conductivity, but plays a fundamental role in controlling the Li-ion migration mobility. To investigate this effect in further details, the diffusion coefficient (D_{Li}^+) and the average migration distance ($<r_{Li}^+>$) of Li$^+$ in bulk are determined using Equations 9 and 10 (see the method details section), respectively. Results of D_{Li}^+ and $<r_{Li}^+>$ are reported in Figures 1D and S5 of supplemental information, respectively, and summarized in Table S1. This is a clear and definitive argument that the presence of carbon is fundamental, not only for the electrical conductivity enhancement (*i.e.*, carbon as electron collector), but also for the Li-ion diffusion. Unlike the state of the art,[12,16,20] two innovative and unconventional concepts are given here: (1) The data obtained are not contaminated by the wetting of the electrolyte; and (2) not only the addition of carbon can improve the Li-ion mobility by two orders of magnitude, but the type of carbon can further boost the dynamics by two extra orders of magnitude in the case of carbon nanotubes.

Positron annihilation spectroscopy studies

To shed light on the interaction between Li-ions and the carbon/cathode grain interface, an antimatter quantum probe, the positron, is used. A relevant difference in the positron lifetime spectra is shown in Figure 2, the *No C* cathode can be represented with only one lifetime component, whereas the carbon coated cathodes possesses two. A more accurate analysis using a deconvolution method[24] is illustrated in Table 1. The first lifetime component has a similar value in all cases (145–165 ps).[25] Theoretical calculations give a positron lifetime of 131 ps in the LCO bulk crystal.[26] The measured values indicate that τ_1, which in carbon coated samples is increased after ball milling, is an unresolved lifetime component that includes both the bulk as well as the vacancy-like defect contributions. However, the most significant difference in Figure 2 is the appearance of the second lifetime component, averaging about 330 ps, whose intensity I_2 depends on the carbon type (inset of Figure 2 and Table 1). It is easy to attribute this second component to carbon at the

Table 1. Positron lifetime components, relative intensities, average positron lifetime and S parameter ("asymptotic" value, Figure 3C) obtained in the LCO cathodes

Cathode	τ_1 (ps)	τ_2 (ps)	I_1 (%)	I_2 (%)	$\bar{\tau}$ (ps)	S parameter
No C	145 (2)	–	100	–	145 (2)	0.432 (2)
SP	154 (2)	319 (2)	74 (2)	26 (2)	197 (3)	0.478 (2)
XC	165 (2)	347 (3)	63 (2)	37 (2)	231 (4)	0.488 (3)
NT	163 (2)	332 (2)	59 (2)	41 (2)	233 (3)	0.489 (3)

grain boundary.[27,28] Nevertheless, considering that the vast majority of the cathode material volume fraction is occupied by LCO crystals, almost all positrons have been implanted inside them. After thermalization positrons can diffuse inside the defected grains only tens of nanometers compared to the grain dimension (~1-2 μm).[26] Therefore, almost all positrons are expected to annihilate inside the grain, as found in the *No C* cathode. Positrons are in a single state associated with the crystal in the carbon-free coated LCO, whereas positrons are in two states in the carbon-coated crystals.

To understand the nature of this second quantum state that gives rise to the second lifetime component, Coincidence Doppler Broadening (CDB) measurements were performed. Figure 3 shows the CDB results (see the method details section). The annihilation peak intensity $I(p_L)$ and the momentum distributions $N(p_L)$ are presented in Figures 3A, B and D, 3C illustrates the S parameter as a function of the positron implantation energy. This parameter mainly describes the annihilation of positrons with valence electrons.[29] S parameter values in the bulk (at ~17 keV) are quite different for cathodes with and without carbon. The same tendency is observed for the average positron lifetime $\bar{\tau}$ (Table 1). To shed light on the nature of the second quantum state, $N(p_L)$ data of Figures 3B and 3D provides the cathode electrons distribution (centered around the Fermi momentum[30]) supplying the chemical environment information at the annihilation sites. The $N(p_L)$ carbon-free LCO distribution is explained by oxygen 2p character.[31,32] Instead, the carbon-coated cathodes distributions are clearly shifted to the left, in the direction of the carbon side (black histogram) which is described by the carbon 2p orbitals. In fact, it is possible to reproduce the carbon-coated distributions $N(p_L)$ using a linear combination of the carbon and the *No C* distributions consistent with the lifetime results (green, red and black histograms in Figures 3B and 3D, see details in method details section). Therefore, the origin of the second quantum state is rationalized by the important fraction of positrons that, once implanted in the grain, spill over onto the carbon. This requires an attractive potential at the interface created by the carbon presence.

Several studies establish that LCO grains have semiconducting characteristics with a variable bandgap (~1-3 eV) because of the possible inclusion of disordered phases.[34,35] In addition, Tukamoto et al.[36] suggest that the LCO growth conditions favor the presence of a small concentration of Co^{4+}, so LCO exhibits p-type semi-conductivity. Beyond this fact, the positron attraction by the carbon capping layer leads us to conclude that there are two possible interactions at the carbon/LCO interface after ball-milling:

(i) A Schottky junction carbon/LCO(n-type) is formed (a detailed description of the Schottky junction is discussed in the method details section). The first Schottky barrier in a carbon/semiconductor was observed by Tongay et al.[37] In this case the negative charges are localized in the carbon coating,[38] which attract positrons. A spheroidal Schottky barrier is expected which could change the band structure of the crystal.[39]

(ii) A carbon/LCO ohmic contact is formed, in this case the positive charge/ion inside the crystal forms a negative image charge at the carbon coating layer that in turn attracts the positrons, as predicted by Rivas et al.[40] In fact, Shi et al.[41,42] have shown that "positrons" are a highly sensitive probe at the coating/semiconductor quantum dots interface.[43] Positron surface states spilling over at this interface have been explained within the Weighted Density Approximation. These states are bound to the interface by a long-distance image potential.[42]

PAS results show clear evidence that positrons are attracted by the carbon coating layers. These data seem to be inconsistent with a recent electrical characterization performed in an analogous system showing the existence of a carbon/LCO(p-type) Schottky barrier.[44] It is important to keep in mind that PAS does not
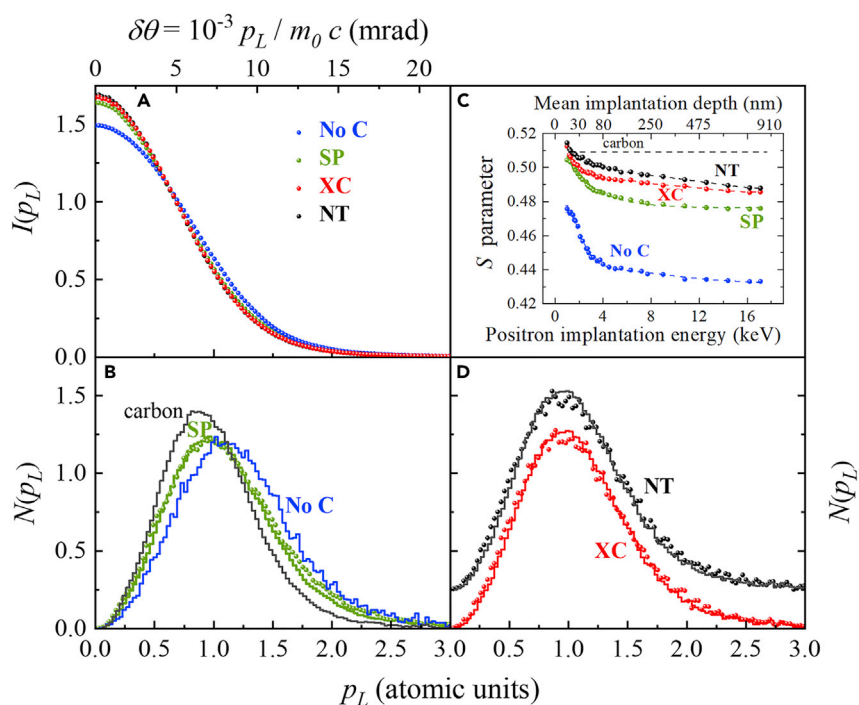
Figure 3. (A) Coincidence Doppler broadening of the annihilation radiation of the studied cathode materials
Distribution of the annihilation peak intensity $I(p_L)$ (normalized in area) as a function of the momentum p_L of the annihilation pair in the longitudinal direction of detection.

(B and D) Momentum distribution $N(p_L)$ associated with the high momentum electron contribution, *i.e.*, the chemical fingerprint of the annihilation site (*NT* distribution is translated adding 0.25 $N(p_L)$ units to prevent overlapping).

(C) S parameter evolution as a function of the positron implantation energy (or mean implantation depth, upper frame) in LCO cathodes and in carbon (black dashed line). The dashed lines through the experimental data in panel c correspond to a VEPFIT fit.[33]

affect the interface charge configuration. Here, we use a single positron at the time as a quantum analogue of the Li-ion. Its delocalized wavefunction can sense the interface globally. Moreover, when the number of positron surface states is largely populated, this value becomes an accurate descriptor for the Li-ion ability to hop outside the nanoparticle. Therefore, it is not surprising that the lifetime intensity I_2 could be a suitable descriptor for Li-ion conductivity.

Battery test

The effect of carbon coating on the electrochemical properties of the LCO material is provided by implementing the cathode mixes here proposed into a battery prototype device, which is cycled under operative conditions. Results are shown in Figure S8 of supplemental information. At low current rates (*i.e.*, 0.5 and 1C), as the specific capacity delivered by each battery is within the experimental error, the discrepancy between the different cathodes is not evident. As expected, at moderate high C-rates (*i.e.*, 2 and 4C) the performance of the prototype drops down in the order NT > XC > SP, confirming the trend revealed in these systems by both BES and PAS spectroscopies. It should be noticed that these latter techniques are useful for predicting the long-term stability during cycling of cathodic materials, thus demonstrating that when LCO is coated with NT, XC and SP carbon their retained specific capacity decreases in the order NT > XC > SP.

Conclusions

Clearly, there is an excellent agreement between BES and PAS results. Both effective mobile Li-ion number $n_{Li^+ eff}$ (Figure 1C) and the number of positrons reaching the carbon capping layer (I_2 in the inset of Figure 2) are influenced by the carbon coating layer type. Moreover, BES and PAS measurements can be explained by an attractive potential at the carbon/oxide interface that acts on Li-ions and positrons. Besides, a crucial

influence on the Li$^+$ diffusion coefficient D_{Li}^+ (Figure 1D) is observed. All these data reveal that the carbon/oxide interface is the key region for understanding Li-ion mobility during charge and discharge processes. Indeed, the interface region is the ionic exchange zone that can be optimized to boost the charge and discharge rate of ion batteries. Our work shows that positrons can be used as quantum simulators to probe the quality of crucial interfaces in batteries. This unique quantum information tool can be therefore adopted by the battery industry for quality inspection.

Limitations of the study

The studies on these electrode materials can be further integrated performing BES and PAS investigations on functional materials at different state of charge and different type of coating.

STAR★METHODS

Detailed methods are provided in the online version of this paper and include the following:

- KEY RESOURCES TABLE
- RESOURCE AVAILABILITY
  - Lead contact
  - Materials availability
  - Data and code availability
- METHOD DETAILS
  - Reagents
  - Electrode preparation
  - Broadband Electrical Spectroscopy studies
  - Positron annihilation lifetime spectroscopy
  - Doppler broadening spectroscopy
  - Battery tests
  - Broadband electrical spectroscopy theory
  - Positron annihilation spectroscopy compatibility tests
  - Linear combination of annihilating contributions
  - Schottky junction

SUPPLEMENTAL INFORMATION

Supplemental information can be found online at https://doi.org/10.1016/j.isci.2022.105794.

AUTHOR CONTRIBUTIONS

Sample preparation and BES experiments, G.P., K.V., and V.D.N.; PAS experiments and data analysis A.C., X.L., R.F., V.T., and M.Z.; Theoretical interpretation, B.B. All authors discussed the results and contributed to the planning and writing the manuscript. All authors have read and agreed to the published version of the manuscript.

DECLARATION OF INTERESTS

The authors declare no competing interests.

REFERENCES

1. Merryweather, A.J., Schnedermann, C., Jacquet, Q., Grey, C.P., and Rao, A. (2021). Operando optical tracking of single-particle ion dynamics in batteries. Nature *594*, 522–528. https://doi.org/10.1038/s41586-021-03584-2.

2. Zhu, G., Tian, X., Tai, H.-C., Li, Y.-Y., Li, J., Sun, H., Liang, P., Angell, M., Huang, C.-L., Ku, C.-S., et al. (2021). Rechargeable Na/Cl$_2$ and Li/Cl$_2$ batteries. Nature *596*, 525–530. https://doi.org/10.1038/s41586-021-03757-z.

3. Pagot, G., Bandiera, M., Vezzù, K., Migliori, A., Bertoncello, R., Negro, E., Morandi, V., and Di Noto, V. (2020). High valence transition metal-doped olivine cathodes for superior energy and fast cycling lithium batteries. J. Mater. Chem. *8*, 25727–25738. https://doi.org/10.1039/d0ta06865a.

4. Grande, L., Paillard, E., Hassoun, J., Park, J.-B., Lee, Y.-J., Sun, Y.-K., Passerini, S., and Scrosati, B. (2015). The lithium/air battery: still an emerging system or a practical reality? Adv. Mater. *27*, 784–800. https://doi.org/10.1002/adma.201403064.

5. Pagot, G., Bertasi, F., Nawn, G., Negro, E., Carraro, G., Barreca, D., Maccato, C., Polizzi, S., and Di Noto, V. (2015). High-performance olivine for lithium batteries: effects of Ni/Co doping on the properties of LiFe$_\alpha$Ni$_\beta$Co$_\gamma$PO$_4$ cathodes. Adv. Funct. Mater. *25*, 4032–4037. https://doi.org/10.1002/adfm.201501167.

6. Scrosati, B., and Garche, J. (2010). Lithium batteries: status, prospects and future. J. Power Sources *195*, 2419–2430. https://doi.org/10.1016/j.jpowsour.2009.11.048.

7. Zaghib, K., Mauger, A., Groult, H., Goodenough, J.B., and Julien, C.M. (2013). Advanced electrodes for high power Li-ion batteries. Materials *6*, 1028–1049. https://doi.org/10.3390/ma6031028.

8. Giorgetti, M., Mignani, A., Aquilanti, G., Conti, P., Fehse, M., and Stievano, L. (2016). Structural and electronic studies of metal hexacyanoferrates based cathodes for Li rechargeable batteries. J. Phys, Conf. Ser. *712*, 012127. https://doi.org/10.1088/1742-6596/712/1/012127.

9. Zhang, B., Cheng, L., Deng, P., Xiao, Z., Ming, L., Zhao, Y., Xu, B., Zhang, J., Wu, B., and Ou, X. (2021). Effects of transition metal doping on electrochemical properties of single-crystalline LiNi$_{0.7}$Co$_{0.1}$Mn$_{0.2}$O$_2$ cathode materials for lithium-ion batteries. J. Alloys Compd. *872*, 159619. https://doi.org/10.1016/j.jallcom.2021.159619.

10. Seher, J., and Fröba, M. (2021). Shape matters: the effect of particle morphology on the fast-charging performance of LiFePO$_4$/C nanoparticle composite electrodes. ACS Omega *6*, 24062–24069. https://doi.org/10.1021/acsomega.1c03432.

11. Park, M., Zhang, X., Chung, M., Less, G.B., and Sastry, A.M. (2010). A review of conduction phenomena in Li-ion batteries. J. Power Sources *195*, 7904–7929. https://doi.org/10.1016/j.jpowsour.2010.06.060.

12. Kwon, N., Mouck-Makanda, D., and Fromm, K. (2018). A review: carbon additives in LiMnPO$_4$- and LiCoO$_2$-based cathode composites for lithium ion batteries. Batteries *4*, 50. https://doi.org/10.3390/batteries4040050.

13. Pandit, B., Fraisse, B., Stievano, L., Monconduit, L., and Sougrati, M.T. (2022). Carbon-coated FePO$_4$ nanoparticles as stable cathode for Na-ion batteries: a promising full cell with a Na$_{15}$Pb$_4$ anode. Electrochim. Acta *409*, 139997. https://doi.org/10.1016/j.electacta.2022.139997.

14. Dominko, R., Gaberscek, M., Bele, M., Mihailovic, D., and Jamnik, J. (2007). Carbon nanocoatings on active materials for Li-ion batteries. J. Eur. Ceram. Soc. *27*, 909–913. https://doi.org/10.1016/j.jeurceramsoc.2006.04.133.

15. Joachin, H., Kaun, T.D., Zaghib, K., and Prakash, J. (2009). Electrochemical and thermal studies of carbon-coated LiFePO$_4$ cathode. J. Electrochem. Soc. *156*, A401. https://doi.org/10.1149/1.3106121.

16. Chen, Z., Qin, Y., Amine, K., and Sun, Y.K. (2010). Role of surface coating on cathode materials for lithium-ion batteries. J. Mater. Chem. *20*, 7606–7612. https://doi.org/10.1039/C0JM00154F.

17. Li, H., and Zhou, H. (2012). Enhancing the performances of Li-ion batteries by carbon-coating: present and future. Chem. Commun. *48*, 1201–1217. https://doi.org/10.1039/C1CC14764A.

18. Kang, B., and Ceder, G. (2009). Battery materials for ultrafast charging and discharging. Nature *458*, 190–193. https://doi.org/10.1038/nature07853.

19. Gaabour, L.H. (2021). Study of the structural, AC electrical conductivity, electric modulus, and dielectric properties of novel PVDF/LiCoO$_2$ nanocomposites for Li-ion batteries. AIP Adv. *11*, 095114. https://doi.org/10.1063/5.0065379.

20. Cao, Q., Zhang, H.P., Wang, G.J., Xia, Q., Wu, Y.P., and Wu, H.Q. (2007). A novel carbon-coated LiCoO$_2$ as cathode material for lithium ion battery. Electrochem. Commun. *9*, 1228–1232. https://doi.org/10.1016/j.elecom.2007.01.017.

21. Zhou, A., Dai, X., Lu, Y., Wang, Q., Fu, M., and Li, J. (2016). Enhanced interfacial kinetics and high-voltage/high-rate performance of LiCoO$_2$ cathode by controlled sputter-coating with a nanoscale Li$_4$Ti$_5$O$_{12}$ ionic conductor. ACS Appl. Mater. Interfaces *8*, 34123–34131. https://doi.org/10.1021/acsami.6b11630.

22. Pagot, G., Bertasi, F., Nawn, G., Negro, E., Bach Delpeuch, A., Vezzù, K., Cristofori, D., and Di Noto, V. (2017). Effect of graphite and copper oxide on the performance of high potential Li[Fe$_{1/3}$Ni$_{1/3}$Co$_{1/3}$]PO$_4$ olivine cathodes for lithium batteries. Electrochim. Acta *225*, 533–542. https://doi.org/10.1016/j.electacta.2016.12.149.

23. Vezzù, K., García-González, E., Pagot, G., Urones-Garrote, E., Sotomayor, M.E., Varez, A., and Di Noto, V. (2022). Effect of relaxations on the conductivity of La$_{1/2+1/2x}$Li$_{1/2-1/2x}$Ti$_{1-x}$Al$_x$O$_3$ fast ion conductors. Chem. Mater. *34*, 5484–5499. https://doi.org/10.1021/acs.chemmater.2c00459.

24. Kansy, J. (1996). Microcomputer program for analysis of positron annihilation lifetime spectra. Nucl. Instrum. Methods Phys. Res. Sect. A Accel. Spectrom. Detect. Assoc. Equip. *374*, 235–244. https://doi.org/10.1016/0168-9002(96)00075-7.

25. Pagot, G., Toso, V., Barbiellini, B., Ferragut, R., and Di Noto, V. (2021). Positron annihilation spectroscopy as a diagnostic tool for the study of LiCoO$_2$ cathode of lithium-ion batteries. Condensed Matter *6*, 28. https://doi.org/10.3390/condmat6030028.

26. Barbiellini, B., and Kuriplach, J. (2017). Advanced characterization of lithium battery materials with positrons. J. Phys.Conf. Ser. *791*, 012016. https://doi.org/10.1088/1742-6596/791/1/012016.

27. Eren, B., Eren, E., Guney, M., Jean, Y., and Van Horn, J.D. (2020). Positron annihilation lifetime spectroscopy study of polyvinylpyrrolidone-added polyvinylidene fluoride membranes: investigation of free volume and permeation relationships. J. Polym. Sci. *58*, 589–598. https://doi.org/10.1002/pol.20190031.

28. Onitsuka, T., Ohkubo, H., Takenaka, M., Tsukuda, N., and Kuramoto, E. (2000). Positron lifetime calculation for defects and defect clusters in graphite. J. Nucl. Mater. *283–287*, 922–926. https://doi.org/10.1016/S0022-3115(00)00381-0.

29. Koushik, D., Naziris, F., Melskens, J., Nusteling, A., Zardetto, V., Schut, H., Kessels, W.M.M., Eijt, S.W.H., and Creatore, M. (2019). On the effect of atomic layer deposited Al$_2$O$_3$ on the environmental degradation of hybrid perovskite probed by positron annihilation spectroscopy. J. Mater. Chem. C *7*, 5275–5284. https://doi.org/10.1039/C8TC06330C.

30. Stewart, A.T. (1957). Momentum distribution of metallic electrons by positron annihilation. Can. J. Phys. *35*, 168–183. https://doi.org/10.1139/p57-020.

31. Barbiellini, B., Suzuki, K., Orikasa, Y., Kaprzyk, S., Itou, M., Yamamoto, K., Wang, Y.J., Hafiz, H., Yamada, R., Uchimoto, Y., et al. (2016). Identifying a descriptor for d-orbital delocalization in cathodes of Li batteries based on x-ray Compton scattering. Appl. Phys. Lett. *109*, 073102. https://doi.org/10.1063/1.4961055.

32. Hafiz, H., Suzuki, K., Barbiellini, B., Tsuji, N., Yabuuchi, N., Yamamoto, K., Orikasa, Y., Uchimoto, Y., Sakurai, Y., Sakurai, H., et al. (2021). Tomographic reconstruction of oxygen orbitals in lithium-rich battery materials. Nature *594*, 213–216. https://doi.org/10.1038/s41586-021-03509-z.

33. Veen, A.v., Schut, H., Vries, J.d., Hakvoort, R.A., and Ijpma, M.R. (1991). Analysis of

positron profiling data by means of ''VEPFIT. AIP Conf. Proc. *218*, 171–198. https://doi.org/10.1063/1.40182.

34. Czyżyk, M.T., Potze, R., and Sawatzky, G.A. (1992). Band-theory description of high-energy spectroscopy and the electronic structure of LiCoO₂. Phys. Rev. B Condens. Matter *46*, 3729–3735. https://doi.org/10.1103/PhysRevB.46.3729.

35. Radha, S.K., Lambrecht, W.R.L., Cunningham, B., Grüning, M., Pashov, D., and van Schilfgaarde, M. (2021). Optical response and band structure of LiCoO₂ including electron-hole interaction effects. Phys. Rev. B *104*, 115120. https://doi.org/10.1103/PhysRevB.104.115120.

36. Tukamoto, H., and West, A.R. (1997). Electronic conductivity of LiCoO₂ and its enhancement by magnesium doping. J. Electrochem. Soc. *144*, 3164–3168. https://doi.org/10.1149/1.1837976.

37. Tongay, S., Schumann, T., and Hebard, A.F. (2009). Graphite based Schottky diodes formed on Si, GaAs, and 4H-SiC substrates. Appl. Phys. Lett. *95*, 222103. https://doi.org/10.1063/1.3268788.

38. Di Bartolomeo, A. (2016). Graphene Schottky diodes: an experimental review of the rectifying graphene/semiconductor heterojunction. Phys. Rep. *606*, 1–58. https://doi.org/10.1016/j.physrep.2015.10.003.

39. Malagù, C., Guidi, V., Stefancich, M., Carotta, M.C., and Martinelli, G. (2002). Model for Schottky barrier and surface states in nanostructured n-type semiconductors. J. Appl. Phys. *91*, 808–814. https://doi.org/10.1063/1.1425434.

40. Preciado Rivas, M.R., Moshayedi, M., and Mišković, Z.L. (2021). On the role of the energy loss function on the image force on a charge moving over supported graphene. J. Appl. Phys. *130*, 173103. https://doi.org/10.1063/5.0071042.

41. Shi, W., Callewaert, V., Barbiellini, B., Saniz, R., Butterling, M., Egger, W., Dickmann, M., Hugenschmidt, C., Shakeri, B., Meulenberg, R.W., et al. (2018). Nature of the positron state in CdSe quantum dots. Phys. Rev. Lett. *121*, 057401. https://doi.org/10.1103/PhysRevLett.121.057401.

42. Shi, W., Eijt, S.W.H., Suchand Sandeep, C.S., Siebbeles, L.D.A., Houtepen, A.J., Kinge, S., Brück, E., Barbiellini, B., and Bansil, A. (2016). Ligand-surface interactions and surface oxidation of colloidal PbSe quantum dots revealed by thin-film positron annihilation methods. Appl. Phys. Lett. *108*, 081602. https://doi.org/10.1063/1.4942609.

43. Eijt, S.W.H., Barbiellini, B., Houtepen, A.J., Vanmaekelbergh, D., Mijnarends, P.E., and Bansil, A. (2007). Positron studies of surfaces, structure and electronic properties of nanocrystals. Phys. Status Solidi *4*, 3883–3888. https://doi.org/10.1002/pssc.200675753.

44. Maeda, Y., Taguchi, N., and Sakaebe, H. (2021). Analysis of LiCoO₂ electrodes through principal component analysis of current-voltage datacubes measured using atomic force microscopy. J. Vac. Sci. Technol. B *39*, 012402. https://doi.org/10.1116/6.0000695.

45. Palomares, V., Goñi, A., Muro, I.G.d., de Meatza, I., Bengoechea, M., Cantero, I., and Rojo, T. (2010). Conductive additive content balance in Li-ion battery cathodes: commercial carbon blacks vs. in situ carbon from LiFePO₄/C composites. J. Power Sources *195*, 7661–7668. https://doi.org/10.1016/j.jpowsour.2010.05.048.

46. Ferragut, R. (2012). Atomic fraction around defects associated with nanoparticles in Al-Cu-Mg alloys. Phys. B Condens. Matter *407*, 2676–2683. https://doi.org/10.1016/j.physb.2012.02.008.

47. Barucca, G., Ferragut, R., Lussana, D., Mengucci, P., Moia, F., and Riontino, G. (2009). Phase transformations in QE22 Mg alloy. Acta Mater. *57*, 4416–4425. https://doi.org/10.1016/j.actamat.2009.06.003.

48. Rosa, C.F.A.E., and Capelas de Oliveira, E. (2015). Relaxation equations: fractional models. J. Phys. Math. *6*, 1–7. https://doi.org/10.4172/2090-0902.1000146.

49. Di Noto, V., Giffin, G.A., Vezzù, K., Piga, M., and Lavina, S. (2012). Broadband dielectric spectroscopy: a powerful tool for the determination of charge transfer mechanisms in ion conductors. In Solid State Proton Conductors, P. Knauth and M.L.D. Vona, eds., pp. 109–183.

50. Chełkowski, A. (1980). Dielectric Physics (PWN-Polish Scientific Publishers).

51. Strobl, G. (2007). The Physics of Polymers, 3rd Edition (Springer). https://doi.org/10.1007/978-3-540-68411-4.

52. Runt, J.P., and Fitzgerald, J.J. (1997). Dielectric Spectroscopy of Polymeric Materials: Fundamentals and Application, 1st Edition (American Chemical Society). https://doi.org/10.1021/ja975608v.

53. Debye, P. (1929). Polar Molecules (The Chemical Catalog Company).

54. Cole, K.S., and Cole, R.H. (1941). Dispersion and absorption in dielectrics I. Alternating current characteristics. J. Chem. Phys. *9*, 341–351. https://doi.org/10.1063/1.1750906.

55. Davidson, D.W., and Cole, R.H. (1950). Dielectric relaxation in glycerine. J. Chem. Phys. *18*, 1417. https://doi.org/10.1063/1.1747496.

56. Havriliak, S., and Negami, S. (2007). A complex plane analysis of α-dispersions in some polymer systems. J. Polym. Sci. C. Polym. Symp. *14*, 99–117. https://doi.org/10.1002/polc.5070140111.

57. Pagot, G., Garaga, M., Jadhav, A.L., O'Donnell, L.F., Vezzù, K., Itin, B., Messinger, R.J., Greenbaum, S.G., and Di Noto, V. (2022). Interplay between coordination, dynamics, and conductivity mechanism in Mg/Al-catenated ionic liquid electrolytes. J. Power Sources *524*, 231084. https://doi.org/10.1016/j.jpowsour.2022.231084.

58. Pagot, G., Vezzù, K., Martinez-Cisneros, C.S., Antonelli, C., Levenfeld, B., Varez, A., Sanchez, J., and Di Noto, V. (2021). Interplay between conductivity, matrix relaxations and composition of Ca-polyoxyethylene polymer electrolytes. Chemelectrochem *8*, 2459–2466. https://doi.org/10.1002/celc.202100475.

59. Pagot, G., Tonello, S., Vezzù, K., and Di Noto, V. (2018). A new glass-forming electrolyte based on lithium glycerolate. Batteries *4*, 41. https://doi.org/10.3390/batteries4030041.

60. Nawn, G., Vezzù, K., Bertasi, F., Pagot, G., Pace, G., Conti, F., Negro, E., and Di Noto, V. (2018). Electric response and conductivity mechanism reciprocity in H₃PO₄-doped Polybenzimidazole-4N-ZrO₂ nanocomposite membranes. Solid State Ionics *320*, 172–176. https://doi.org/10.1016/j.ssi.2018.03.003.

61. Bertasi, F., Vezzù, K., Nawn, G., Pagot, G., and Di Noto, V. (2016). Interplay between structure and conductivity in 1-Ethyl-3-methylimidazolium tetrafluoroborate/(δ-MgCl₂)f electrolytes for magnesium batteries. Electrochim. Acta *219*, 152–162. https://doi.org/10.1016/j.electacta.2016.09.091.

62. Pagot, G., Bertasi, F., Vezzù, K., Nawn, G., Pace, G., Nale, A., and Di Noto, V. (2018). Correlation between properties and conductivity mechanism in poly(vinyl alcohol)-based lithium solid electrolytes. Solid State Ionics *320*, 177–185. https://doi.org/10.1016/j.ssi.2018.03.001.

63. Pagot, G., Bertasi, F., Vezzù, K., Sepehr, F., Luo, X., Nawn, G., Negro, E., Paddison, S.J., and Noto, V.D. (2017). Three-dimensional catenated 1-ethyl-3-methylimidazolium halotitanate ionic liquid electrolytes for electrochemical applications. Electrochim. Acta *246*, 914–923. https://doi.org/10.1016/j.electacta.2017.06.089.

64. Bonanos, N., Steele, B.C.H., Butler, E.P., Macdonald, J.R., Johnson, W.B., Worrell, W.L., Niklasson, G.A., Malmgren, S., Strømme, M., Sundaram, S.K., et al. (2018). Applications of impedance spectroscopy. In Impedance Spectroscopy, E. Barsoukov and J.R. Macdonald, eds., pp. 175–478.

65. Schütt, H., and Gerdes, E. (1992). Space-charge relaxation in ionically conducting glasses. II. Free carrier concentration and mobility. J. Non-Cryst. Solids *144*, 14–20. https://doi.org/10.1016/S0022-3093(05)80378-3.

66. Dubov, L., Akmalova, Y., Stepanov, S., Shtotsky, Y., and Shtotsky, Y. (2017). Evaluation of positron implantation profiles in various materials for ²²Na source. Acta Phys. Pol. *132*, 1482–1486.

67. Murty, R.C. (1965). Effective atomic numbers of heterogeneous materials. Nature *207*, 398–399. https://doi.org/10.1038/207398a0.

68. Arifov, P.U., Grupper, A.R., and Alimkulov, H. (1982). Coefficients of positron mass absorption and backscattering. In Positron Annihilation, P.G. Coleman, S.C. Sharma, and L.M. Diana, eds., pp. 699–701.

69. Aers, G.C., Marshall, P.A., Leung, T.C., and Goldberg, R.D. (1995). Defect profiling in

multilayered systems using mean depth scaling. Appl. Surf. Sci. *85*, 196–209. https://doi.org/10.1016/0169-4332(94)00332-7.

70. Cesano, F., Uddin, M.J., Lozano, K., Zanetti, M., and Scarano, D. (2020). All-carbon conductors for electronic and electrical wiring applications. Front. Mater. *7*. https://doi.org/10.3389/fmats.2020.00219.

71. Rut'kov, E.V., Afanas'eva, E.Y., and Gall, N.R. (2020). Graphene and graphite work function depending on layer number on Re. Diam. Relat. Mater. *101*, 107576. https://doi.org/10.1016/j.diamond.2019.107576.

72. Schuld, S., Hausbrand, R., Fingerle, M., Jaegermann, W., and Weitzel, K.-M. (2018). Experimental studies on work functions of Li^+ ions and electrons in the battery electrode material $LiCoO_2$: a thermodynamic cycle combining ionic and electronic structure. Adv. Energy Mater. *8*, 1703411. https://doi.org/10.1002/aenm.201703411.

STAR★METHODS

KEY RESOURCES TABLE

REAGENT or RESOURCE	SOURCE	IDENTIFIER
Chemicals, peptides, and recombinant proteins		
Lithium cobalt oxide (LCO)	Nippon Chemical Industrial	CELLSEED(Lithium-Cobalt Oxide)
Carbon black, Super P (SP)	Alfa Aesar	H30253
Carbon black (XC)	CARBOCROM	XC-72R
Multi-walled carbon nanotubes (NT)	US Research Nanomaterials	US4300
Poly(vinylidene fluoride)	Sigma-Aldrich	182,702
1-methyl-2- pyrrolidone (NMP)	Sigma-Aldrich	328,634
Lithium hexafluorophosphate solution	Sigma-Aldrich	746,711
Lithium Chips	MTI	EQ-Lib-LiC
Aluminum Foil Substrate	MTI	EQ-bcaf-15u-180

RESOURCE AVAILABILITY

Lead contact

Further information and requests for resources should be directed to and will be fulfilled by the lead contact, V.D.N. (vito.dinoto@unipd.it).

Materials availability

This study did not generate new unique reagents.

Data and code availability

- All data reported in this Paper will be shared by the lead contact upon request.

- This paper does not report original code.

- Any additional information required to reanalyze the data reported in this paper is available from the lead contact upon request.

METHOD DETAILS

Reagents

The $LiCoO_2$ (LCO) cathode was obtained from Nippon Chemical Industrial. Three different types of carbon conductive material were used in this work: (i) carbon black (Super P, the abbreviations are presented in the next paragraph), purchased from Alfa Aesar; (ii) XC-72R carbon black nanospheres (*ca.* 30-50 nm in diameter), provided as a courtesy by Carbocrom srl; and (iii) multi-walled carbon nanotubes (>95%, OD < 7 nm), obtained from US Research Nanomaterials, Inc. Super P carbon is obtained by partial combustion or by thermal decomposition of liquid or gaseous hydrocarbons, and the result is the formation of branched structures and aggregates bigger than 100 nm.[45] The BET surface area is 57-67 $m^2 g^{-1}$. XC-72R nanoparticles tend to maintain their nanosphere morphology and not to aggregate forming larger agglomerates. The BET surface area is *ca.* 220 $m^2 g^{-1}$. The multiwalled carbon nanotubes are prepared by means of the CVD method. They have an outer diameter <7 nm and an inner diameter of 2-5 nm. The length of each nanotube is 10-30 μm and their BET surface area is 500 $m^2 g^{-1}$. The polyvinyl difluoride (PVDF, Sigma-Aldrich) binder was suspended in 1-methyl-2- pyrrolidone (NMP, 99.5%, anhydrous, Sigma-Aldrich) at 10 wt % concentration. The battery-grade aluminum foil and lithium metal chips were obtained from MTI. The 1 M $LiPF_6$ in EC/DMC 1:1 V/V electrolyte solution was purchased from Sigma-Aldrich. All materials were used instantly as received. Densities of the LCO, Super P conductive carbon, and PVDF were determined to be 4.9317 ± 0.0003, 2.2375 ± 0.0016, and 1.6870 ± 0.0006 g cm^{-3}, respectively, using an Ultrapyc 1200e gas pycnometer produced by Quantachrome.

Electrode preparation

LCO and each carbon allotrope were grinded together using a planetary ball-miller for 2 h at 500 rpm. Then, an exact amount of the 10 wt % PVDF in NMP suspension was added to each LCO/C mixture in order to prepare a cathodic ink with an LCO:C:PVDF weight composition of 93.75:4.00:2.25. The obtained inks were deposited onto the Al foil by means of a doctor-blade automatic system. The cathodic layers were dried overnight at 70°C and for 24 h in vacuum at 120°C. A cathode electrode without the addition of any type of carbon has been prepared by simply mixing LCO and PVDF (97.75:2.25 wt %). Identical deposition and drying processes as described above were carried out in this case. Summarizing, four different cathode electrodes were obtained and labeled according to their carbon allotrope constituents: (i) "*NoC*", without carbon; (ii) "*SP*", with carbon Super P; (iii) "*XC*", containing carbon nanospheres; and (iv) "*NT*", containing carbon nanotubes. All the cathode electrodes have a thickness of 120 ± 10 μm. The morphology and element distribution of the obtained cathode electrodes is investigated using a JEOL JSM 7900F HR-FEG-SEM. The cathode electrodes were attached on an aluminum support holder by means of a carbon adhesive tape and placed into the instrument. An accelerating voltage of 15 kV was applied during the measurements. EDS mapping is performed using an Oxford Instrument ULTIM MAX 40 probe. Results are shown and discussed in Figures S9 and S10 of supplemental information.

Broadband Electrical Spectroscopy studies

Broadband Electrical Spectroscopy (BES) studies were carried out after drying the samples in vacuum at 120°C for 24 h. The complex permittivity and conductivity spectra were acquired in the frequency range between 0.03 and 10^7 Hz at 25 ± 0.5°C using a Novocontrol Alpha-A analyzer. The cathode electrodes were cut into disks being 13 mm in diameter, sandwiched between two platinum electrodes and placed into a sealed cylindrical Teflon cell. The cell assembly was performed inside an argon-filled glove box in order to avoid moisture contaminations. Experimental data for *SP* and *NT* samples show a strong noise at low frequency (experiments were performed three times to confirm this phenomenon), so these points have been cut off.

Positron annihilation lifetime spectroscopy

The positron annihilation lifetime experiments were performed using a fast–fast coincidence lifetime setup, which employs a time resolution (FWHM) of ~235 ps and a time calibration of 25.35 ps per channel for a multi-channel analyzer (MCA) card. The positron source ^{22}Na (2 μCi) enveloped by two 7.5 μm thick Kapton foils was sandwiched between two pairs of identical cathode samples (see the schematic illustration of the source/sample configuration in Figure S6 in supplemental information). Each layer of the cathode samples has a thickness of 120 ± 10 μm. All lifetime measurements were performed at room temperature (21 ± 1°C) at atmospheric pressure. Each positron lifetime spectrum was recorded on $\sim 4 \times 10^6$ annihilation events, requiring an acquisition time of 36-48 h. The source component of 382 ps associated with annihilations within the Kapton foil was accurately measured with the carbon coating-free cathode with an intensity of 14.0(0.5)%, which were considered constant throughout the analysis with all LCO samples. PALS spectra were fitted using the LT software.[24] The lifetime spectrum obtained in PALS appears as a convolution of instrumental resolution and measured components. The LT program employs certain algorithms to carry out the deconvolution and fitting of the experimental data with optimum parameters, so that each lifetime component can be identified. Generally, after subtraction of the Kapton component, there appear two or three discrete components. In the latter case, $\tau_1 < \tau_2 < \tau_3$ with their corresponding intensities, I_1, I_2 and I_3 can be observed. The goodness parameter of the fit (χ^2/dof) lay between 0.9 and 1.05. The so-called "*spurious*" component τ_3 of about 2.0(0.2) ns has, in general, a very low intensity I_3 (<0.05%) for a smoothly-surfaced metal or semiconductor being measured with the source in question under ideal condition. For a sample with porous or coarse surface, as in the case of the cathode oxide (LCO), the intensity of this component was between 0.2 and 0.4%. A more realistic analysis with one or two lifetime components is presented in this work after subtraction of the source and spurious contributions (see Figure 2). Our estimation indicates that about 98(1)% of the positrons annihilate inside the LCO cathode material (see the positron implantation profile discussion here below).

Doppler broadening spectroscopy

Doppler broadening spectroscopy of the annihilation radiation was used to monitor the microstructure of the studied cathode crystal. Positrons were implanted at various depths in the sample using a variable energy positron beam ranging between 1 and 17 keV. Two HPGe detectors (Ortec, relative efficiency ~50% at

1.33 MeV) were used to measure the spectrum of the annihilation gamma radiation. The measurements were carried out at room temperature ($21 \pm 1°C$) in a vacuum condition ($\sim 10^{-7}$ mbar). The broadening of the 511 keV annihilation peak due to the Doppler effect caused by the motion of the annihilating electrons was characterized by identifying the area around the maximum of the annihilation peak and defining a parameter called S parameter. The S parameter is the fraction of annihilating positron-electron pairs in the energy range within 511 ± 0.85 keV (corresponding to the momenta $|p_L| \leq 0.456$ atomic units), determined by the ratio of the area under the central part of the annihilation peak to the total peak area covering the energy range 511 ± 4.25 keV. The S parameter mainly corresponds to annihilation of positrons with valence electrons moving with low momenta in the sample. To obtain information of the chemical environment at the annihilation site, it is necessary to reduce the background in the high-momentum region of the annihilation peak, which is obtained by adopting the Coincidence Doppler Broadening (CDB) technique. It uses two detectors mounted at 180° from each other working in coincidence in energy and in time. CDB spectra with $\sim 10^7$ total counts were measured with a peak/background ratio of 10^5 to 10^6. The experimental procedure performed in this study is described in detail in the literature.[46]

The distribution of the annihilation peak intensity $I(p_L)$ was obtained by summing the counts in the two-dimensional spectrum represented by the matrix $S(E_1, E_2)$ along the diagonal line $p_L = (E_1 - E_2)/c$, in the interval $1022\ keV - \Delta E < E_1 + E_2 < 1022\ keV + \Delta E$, where $\Delta E = 2.1\ keV$.[47] The intensity $I(p_L)$ of the photons emitted by the annihilating positron-electron pairs are represented in Figure 3A. The energy spectrum of these photons is subject to a Doppler shift, due to the center of mass of the annihilated pairs varying comparatively to the laboratory reference frame. The Doppler effect mainly depends on the velocity distribution of the electrons at the annihilation site. The contribution of positrons to the Doppler effect is negligible because they thermalize at the measurement temperature (at about tens of millielectronvolts in a few picoseconds). Therefore, CDB maps the velocity distribution of electrons in the studied material. In general, a moving center of mass of the annihilating particles with respect to an observer will result in the angle between the photon propagation directions differing from 180° by an amount $\delta\theta$ of an order of v_{CM}/c, where v_{CM} is the velocity of the center of mass of the particles and c is the speed of light. The measurements are performed in the longitudinal direction of the momentum component $p_L = m_0 v_{CML}$ along the axis that passes through the annihilation site inside the studied material and the midpoint between the two HPGe detectors. The measured angular deviation is typically of the order of milliradians, which is proportional to the momentum p_L by $\delta\theta = 10^{-3} \frac{p_L}{m_0 c}$ (mrad), where m_0 is the electron or positron mass. As illustrated in Figure 3, the longitudinal p_L momentum x-axis in atomic units (a.u.) in the lower frame (1 a.u. $\equiv \frac{\hbar}{a_0}$, where $\hbar$ is the Plank's constant h divided by 2π and a_0 is the Bohr's radio). The CDB distributions generally show an inverted parabolic shape at low momentum ($I(p_L) \propto - p_L^2$) associated with the "free" conduction and/or valence electrons up to the Fermi momentum p_F. The distributions also contain a broad and less intense distribution that includes the contribution of core electrons. The experimental measure of $I(p_L)$ is somewhat enlarged by the resolution function $R(p_L)$ that behaves in a Gaussian-like form of shape (FWHM= $3.5 \times 10^{-3} m_0 c$).

From $I(p_L)$ distribution in Figure 3A it is possible to obtain the directional average value of the momentum distribution $N(p_L)$, which facilitates comparing the LCO cathodes coated with and without carbon $N(p_L) = -\kappa\, p_L \frac{dI(p_L)}{dp_L}$, where κ is a constant.[30] $N(p_L)$ provides the distribution of the atomic orbital electrons that reveal information about the chemical environment at the annihilation sites.

Battery tests

Battery studies were performed by cycling a CR2032 coin cell prototype device assembled using a lithium metal anode, a solution of 1 M $LiPF_6$ in EC/DMC 1:1 V/V as electrolyte, and each cathode electrode proposed in this work. The cathode electrodes were cut into disks being 15 mm in diameter. Battery prototypes were cycled between 3.0 and 4.3 V at different C rates (1C = 145 mA g^{-1}). Long-term cycling is performed at 0.5C of current rate.

Broadband electrical spectroscopy theory

In general, materials subjected to an electric field undergo a rearrangement in the distribution of charges and dipole moments hosted in their matrix.[48,49] After the removal of the electric field, dipole moments and charges tend to relocate in their equilibrium position. This latter event is not instantaneous and occurs with a certain delay, which is known as *relaxation time*.[49] All these phenomena are subjected to the Maxwell

theory and are described by the Maxwell equations as time-dependent phenomena.[50] These interactions are macroscopically observed and quantified by means of the BES technique, as they result in the formation of local induced charges on the surface of the material which generate a field known as the *depolarization field*.[50] The number and magnitude of these phenomena are a consequence of the intrinsic properties of the investigated material, which is commonly addressed as its *electric response*. The electric response of a compound is commonly described on the angular frequency (ω, with $\omega = 2\pi f$) in terms of complex permittivity ($\varepsilon^*(\omega)$), complex conductivity ($\sigma^*(\omega)$) and complex impedance ($Z^*(\omega)$).[49] The electric response of a material appropriately fits with the principle of superposition in the linear regime, thus the net response of the system to a stimulus is the sum of the responses of all the events involved in the interactions.[51] In the case of a dielectric or an ion-conducting material, these events are: (i) polarization events, which arise from accumulation of charges at the interfaces between domains (*i.e.*, interdomain polarizations) or materials (*i.e.*, electrode polarizations) characterized by a different permittivity, and from the reorientation of dipole moments of a portion of molecules or crystals[49]; and (ii) dielectric relaxations, which are the exponential decay of the polarizations when the applied external field is removed.[49,52]

The first theoretical model used to describe the electric response of materials was proposed by Debye:[49,53]

$$R_j(\omega) \; = \; \frac{1}{1 + i\omega\tau_j} \tag{Equation 1}$$

$$\varepsilon'(\omega) \; = \; \varepsilon_\infty + \frac{\varepsilon_0 - \varepsilon_\infty}{1 + \omega^2\tau^2} = \varepsilon_\infty + \frac{\Delta\varepsilon}{1 + \omega^2\tau^2} \tag{Equation 2}$$

$$\varepsilon''(\omega) \; = \; \frac{(\varepsilon_0 - \varepsilon_\infty)\omega\tau}{1 + \omega^2\tau^2} \; = \; \frac{\Delta\varepsilon\,\omega\tau}{1 + \omega^2\tau^2} \tag{Equation 3}$$

where $R_j(\omega)$ is the complex relaxation function in the frequency domain of the jth event, and ε' and ε'' are the real and imaginary part of the complex permittivity, respectively. ω is the angular frequency, ε_∞ is the dielectric constant of the sample measured at frequencies so high that the dipole orientational contribution has vanished (electronic contribution), ε_0 is the absolute dielectric permittivity in vacuum conditions, τ is the relaxation time and $\Delta\varepsilon$ is the dielectric total strength ($\varepsilon_0 - \varepsilon_\infty$). Different empirical equations have been proposed starting from the Debye model (*i.e.*, Cole-Cole[54] and Cole-Davidson[55]), which find their general expression in the Havriliak-Negami (HN) model:[56]

$$R_j(\omega) \; = \; \frac{1}{\left(1 + (i\omega\tau_{HN})^\alpha\right)^\beta} \tag{Equation 4}$$

where α and β are empirical parameters ($0 \leq \alpha \leq 1$, $0 \leq \beta \leq 1$). The Debye model can be obtained when $\alpha = \beta = 1$, while for $\beta = 1$ or $\alpha = 1$ the Cole-Cole and Cole-Davidson equations are obtained, respectively. Thus, the HN relaxation function (R_j) in Equation 1 is a combination of the Cole-Cole and Cole-Davidson models. The empirical constants α and β are associated with the shape parameters m and n (symmetric and asymmetric broadening) of complex dielectric functions in a supramolecular system ($m = \alpha$ and $n = \alpha \cdot \beta$).[49] In the case of the electrode and interdomain polarizations, a general equation can be extrapolated from the Maxwell theory and the double-layer model:[49]

$$\varepsilon_k^*(\omega) \; = \; \frac{\sigma_k(i\omega\tau_k)^{\gamma_k}}{i\omega\varepsilon_0[1 + (i\omega\tau_k)^{\gamma_k}]} \tag{Equation 5}$$

where $\varepsilon_k^*(\omega)$ is the complex permittivity of the kth event ($k = EP$ or IP_i for the electrode and interdomain polarizations, respectively), and σ_k and τ_k are its conductivity and relaxation time, respectively. γ_k is the exponential factor of the kth event and accounts for the broadening of the related peak. As discussed above, Equations 4 and 5 can be combined considering the principle of superposition in the linear regime, using one equation for each event observed in the experimental data. The result can be summarized as:[49,57–60]

$$\varepsilon_m^*(\omega) \; = \; -i\left(\frac{\sigma_0}{\omega\varepsilon_0}\right)^N + \frac{\sigma_{EP}(i\omega\tau_{EP})^{\gamma_{EP}}}{i\omega\varepsilon_0[1 + (i\omega\tau_{EP})^{\gamma_{EP}}]} + \sum_{i=1}^{g} \frac{\sigma_{IP,i}(i\omega\tau_{IP,i})^{\gamma_{IP,i}}}{i\omega\varepsilon_0[1 + (i\omega\tau_{IP,i})^{\gamma_{IP,i}}]} + \sum_{f=1}^{h} \frac{\Delta\varepsilon_f}{[1 + (i\omega\tau_f)^{\alpha_f}]^{\beta_f}} + \varepsilon_\infty \tag{Equation 6}$$

$$\sigma_m^*(\omega) \; = \; \frac{(\sigma_0)^N}{(\omega\varepsilon_0)^{N-1}} + \frac{\sigma_{EP}(i\omega\tau_{EP})^{\gamma_{EP}}}{1 + (i\omega\tau_{EP})^{\gamma_{EP}}} + \sum_{i=1}^{g} \frac{\sigma_{IP,i}(i\omega\tau_{IP,i})^{\gamma_{IP,i}}}{1 + (i\omega\tau_{IP,i})^{\gamma_{IP,i}}} + \sum_{f=1}^{h} \frac{i\omega\varepsilon_0\Delta\varepsilon_f}{[1 + (i\omega\tau_f)^{\alpha_f}]^{\beta_f}} + i\omega\varepsilon_0\varepsilon_\infty \tag{Equation 7}$$

where $\varepsilon^*(\omega) = \varepsilon'(\omega) - i\varepsilon''(\omega)$ and $\sigma^*(\omega) = i\omega\varepsilon_0\varepsilon^*(\omega)$.[61] The first term accounts for material conductivity at zero frequency (σ_0) and N is the exponential factor of the direct current.[62,63] The second and third terms are related to the interdomain and the electrode polarizations, where σ_k and τ_k are the conductivity and the relaxation times, respectively. The third term describes the dielectric relaxation phenomena in terms of generalized HN functions, where τ_f is the relaxation time, and α, β and γ are empirical shape parameters.

The actual number and concentration of mobile species ($n_{Li^+,eff}$) can be determined using the following equation:[64,65]

$$n_{Li^+,eff} = \left(\frac{\sigma_{dc}}{\sqrt{\left(\frac{\varepsilon'(\omega_x)}{\varepsilon'_s} - 1 \right) \varepsilon_0 \cdot \varepsilon'_s \cdot \omega_x}} \right)^4 \frac{\varepsilon_0 \cdot \varepsilon'_s \cdot k \cdot T}{e^2 \cdot d^2} \qquad \text{(Equation 8)}$$

where σ_{dc} in our case corresponds to σ_1, ω_x is the angular frequency in the slow regime of the Li$^+$ ions kinematics, and $\varepsilon'(\omega_x)$ is the permittivity value of the material at ω_x. ε'_s is ε_∞ of Equation 6, k is the Boltzmann constant, T the temperature in Kelvin, e the electron charge and d the thickness of the sample.

The diffusion coefficient (D_{Li}) and the average migration distance ($<r_{Li}>$) of Li$^+$ in bulk can be calculated using the following equations:[59]

$$D_{Li} = \frac{\sigma_{dc} \cdot R \cdot T}{n_{Li^+,eff} \cdot F^2} \qquad \text{(Equation 9)}$$

$$<r_{Li}> = \sqrt{6 \cdot D_{Li} \cdot \tau_i} \qquad \text{(Equation 10)}$$

where R and F are the gas universal constant and the Faraday constant, respectively, and τ_i is the relaxation time of the electrode polarization.

Positron annihilation spectroscopy compatibility tests

Positron implantation profile

To maximize the number of positrons implanted in LCO cathodes during the PALS measurements it was necessary to use a multilayer source/sample configuration (Figure S6) with a large lateral dimension (near 1 cm). The LCO cathodes normally used in batteries are deposited on an aluminum foil (d_2= 15 µm). The thicknesses of the studied LCO cathodes is d_1= 120 µm. For the analysis, it is essential to obtain an estimate of the positrons fraction that annihilate in the LCO and Al layers, such intensity in the sample can be identified from the PALS measurements. Due to the mirror symmetry of the configuration used in this work, it is sufficient to perform such analysis on one side of the ^{22}Na source and normalize to the total amount of positrons.

Upon discrimination and subtraction of the source and spurious components from the experimental data, as explained in the *Methods* section, the remaining portion of the positrons are considered as normalized to one hundred percent in the analysis.

To estimate the implantation profile for positrons emitted by a ^{22}Na source through each layer, an approach using the equation proposed by Dubov et al.[66] was used. This profile depends on the mass density and the atomic number (or the effective atomic number[67]). To evaluate the fraction of positrons that effectively annihilate inside the LCO cathode, positron propagation in the layers is considered and the backscattering of positrons at the interfaces. Here we assume that the thickness of each layer z_i is large enough for the implanted positrons to be analyzed with a reliable approximation to effectively annihilate in each layer, *i.e.*, the positron diffusion length $L_+ << z_i$, which is realistic in the studied case and in general, for any thick layers. The backscattering coefficients of positrons incident from the vacuum on a semi-infinite elementary system using the energy spectrum of a ^{22}Na source were estimated by Arifov et al.[68]

Aers et al.[69] proposes an approach to correct the implantation profile $P(z,E)$ of a positron beam by considering that the scattering processes of a positron at a given depth z is affected by the adjacent layer. This correction considers the relative backscattering coefficient, *i.e.*, the difference between the coefficients of the neighboring materials. Using these ideas, we propose a similar approach, instead using the

implantation profile $P(z)$ given by Dubov et al.[66] for the positron energy spectrum of a ^{22}Na source. In general, the implantation profile near an interface with a less dense material is lowered due to reduced back-scattering (see Figure S7, zone I and III). Also, the opposite considerations are true, the profile near an interface with a denser material is increased since the heavy material is a more efficient back-scatterer (see inset of Figure S7, zone II).

Following this approach, the total fraction of positrons thermalized inside Al were estimated to be 1.9(0.6)%. Therefore, it can be safely concluded that, after substracting the source (Kapton) and the spurious components, about 98(1) % of the positrons annihilate within the LCO cathode, and the remaining positrons annihilate in aluminum in our sample configuration.

Linear combination of annihilating contributions

The CDB results of Figures 3B and 3D show that it is possible to reproduce with good approximation the momentum distributions of the carbon coated cathode materials $N(p_L)$ using a lineal combination of the No C cathode $N_{LCO_{No\ C}}(p_L)$ and carbon $N_C(p_L)$ distributions. The histograms in Figures 3B and 3D reproduce with reliable approximation the trend of the experimental data according to:

$$N(p_L) \ = \ \alpha \cdot N_{LCO_{No\ C}}(p_L) + \beta \cdot N_C(p_L) \qquad \text{(Equation 11)}$$

Where α and β are the weights of the quantum states associated with the LCO crystals and the coating carbon ($\alpha + \beta \ = \ 1$). The β values estimated using a best fit for the carbon coated cathodes (Figures 3B and 3D) are presented in Table S2. Furthermore, there is a connection between the measured lifetime and CDB measurements. The integral of the momentum distributions in Figure 3 is proportional to the average annihilation rate λ, the inverse of the average positron lifetime. Therefore, the average lifetime $\overline{\tau}_E$ can be estimated by the following equation as a function of the weight β:[46]

$$\lambda_E \ = \ \overline{\tau}_E^{-1} \cong (1 \ - \ \beta) \cdot \tau_1^{-1} + \beta \cdot \tau_2^{-1} \qquad \text{(Equation 12)}$$

Using the β values and the positron lifetime of τ_1 and τ_2 measured in each sample (Table 1). Comparison of the estimated average lifetimes (Table S2) and measured values (Table 1) showed coherence within experimental and propagation errors. This is a consistency test of two independent approaches that provides a complementary view.

Schottky junction

In results and discussion section were proposed two possible interactions at the carbon/LCO interface. The intimate contact between a conductor (metal or semimetal-carbon or graphene-[70]) and a semiconductor can result in two ideal devices: the Schottky junction or an ohmic junction.

It has been demonstrated that the interface between a contacted conductor with a semiconductor crystal can form a Schottky barrier (SB). Schottky barriers have rectifying characteristics, suitable for the use as a diode. When the barrier is formed, the Fermi levels E_F of the two components tend to correspond to the same value. Consequently, as Figure S11 shows, a bending of the energy bands of the semiconductor near the interface is produced. The bending depends on the characteristics of the conductor (work function Φ_C) and the semiconductor (band gap $E_C \ - \ E_V$ and the difference between the vacuum level and the conduction band at the interface $X \ = \ E_0 \ - \ (E_C + \Phi_i)$).[38] The ideal Schottky barrier height is given by:

$$\Phi_B \ = \ \Phi_C \ - \ X \qquad \text{(Equation 13)}$$

Here, the case study is the carbon/LCO interface. Figure S9 shows in a SEM micrograph the grain distribution of the LCO crystals in compact cathodes. It is noteworthy that given the irregular spheroidal-like LCO grain symmetry and capping of the grain, the classical planar geometry of the Schottky barrier is not valid in this case, therefore the barrier becomes non-conventional. Some efforts were made to treat a spherical-like Schottky barrier,[39] where the calculations predict a dependence between the grain radius R and the thickness of the space charge or depletion region w appears (see Figure S12). In this work, R has an average value between several hundred nanometers and a micrometer (Figure S9). Effects such as flattening of

the band bending and the decrease in the surface state density when w tends to be an appreciable fraction of R have been foreseen.[39] In the case study, the barrier height Φ_B would be nominally of the order of hundreds of millielectronvolts (considering the difference between the graphite work function[71,72] and LCO work function for positive ions[71]). At any rate, a large range of values of the Schottky barrier height as a function of the impurities and defects densities at the junction was observed.[38]

The positron lifetime results (Figure 2 and Table 1) demonstrate that positrons are attracted to the carbon at the grain boundary. Therefore, the presence of a Schottky junction with an LCO n-type, as shown in inset of Figure S12 or a metallic ohmic junction is expected.